Online and Noninvasive Monitoring of Battery Health at Negative-half Cell in All-Vanadium Redox Flow Batteries Using Ultrasound

Litao Yan,[†] Xiaoqin Zang,[†] Zimin Nie, Lirong Zhong, Zhiqun Daniel Deng[*], Wei Wang[*]

Energy and Environment Directorate, Pacific Northwest National Laboratory, Richland 99354, WA, USA

[†]These authors contributed equally.
[*]Corresponding author: zhiqun.deng@pnnl.gov, wei.wang@pnnl.gov

Abstract

Hydrogen evolution is one of the major side reactions that is detrimental to the health of all-vanadium redox flow batteries, especially for long-term cycling. Effective, low-cost, and accurate online prediction and detection methods for hydrogen generation are not yet available. In this work, we designed an online, noninvasive ultrasonic probing approach for monitoring the state of charge (SoC), predicting the hydrogen generation, and detecting hydrogen gas bubbles in anolyte solutions. The technique employs a pulse-echo method to measure the sound speed and the acoustic attenuation coefficient of the anolyte solution. Through static offline experiments and online in operando experiments, we have demonstrated that when hydrogen gas is generated in anolyte solutions, large variations are observed in both sound speed and acoustic attenuation coefficient measurements. We found that the variations of acoustic attenuation coefficient are highly correlated (correlation coefficients >0.9) with the gas flow rate. The designed acoustic method can monitor the SoC of anolyte, predict the hydrogen generation, and detect the presence of gas bubbles in an anolyte solution and, thus, provide information about the state of health for operation and management of flow battery systems.

Keywords

Hydrogen evolution reaction; vanadium redox flow battery; gas bubble detection; ultrasound non-destructive test

1. Introduction

Redox flow batteries are increasingly being considered as a promising energy storage technology that is critical to the national mission of decarbonization. Flow batteries are capable of providing a variety of grid services ranging from modulating the intermittence of the renewable energy, to balancing mismatches between generation and demand, to improving grid resilience during adverse events.[1-5] Among various redox flow chemistries, the all-vanadium redox flow battery (VFB) is the most mature and well-developed flow battery technology that has seen numerous large-scale commercial deployments.[6, 7] Widely regarded as a promising electrochemical system for stationary energy storage, VFBs boasts long cycle lives, high safety, and decoupled energy and power.[2, 5, 8, 9] VFBs employ only vanadium ions with different valence states to store electrical energy following the equations (1), (2), and (3).

$$Negative:\ V^{3+} + e^{-} \rightleftarrows V^{2+}, \quad E^{0} = -0.26\,V\ vs.NHE \qquad (1)$$

$$Positive:\ VO_2^{+} + 2H^{+} + e^{-} \rightleftarrows VO^{2+} + H_2O, \quad E^{0} = 1.00\,V\ vs.NHE \qquad (2)$$

$$Overall:\ VO_2^{+} + 2H^{+} + V^{2+} \rightleftarrows VO^{2+} + H_2O + V^{3+}, \quad E = 1.26\,V \qquad (3)$$

Recently, many efforts have been dedicated to the development of new high-performance vanadium electrolytes, membranes, and electrodes.[10-14] Considering its application for stationary energy storage, long-term stability is of critical importance. One major parasitic side reaction that occurs during the operation of VFBs is the hydrogen evolution reaction (HER) (0 V *vs.* NHE, Equation 4) at the negative electrode. The HER could be thermodynamically triggered by the lower potential (-0.26 V *vs.* NHE) of V^{2+}/V^{3+} redox at the negative electrode (equation 4).[15-19]

$$HER: 2H^+ + 2e^- \rightleftarrows H_2, \quad E^0 = 0\ V\ vs.NHE \quad (4)$$

Several factors can affect hydrogen generation in a practical VFB application. The vanadium electrolyte typically uses concentrated (3–5 M) acid that shifts the potential of HER positively according to equation 5.[17, 20-22]

$$E_{\frac{H^+}{H_2}} = E^0 + \frac{RT}{F}\ln\left(\frac{a_{H^+}}{1}\right)^2 \quad (5)$$

For instance, when the proton concentration is 3 mol/L, $E_{\frac{H^+}{H_2}}$ has a value of ~0.05 V. Meanwhile, flow batteries use carbon-based electrodes to capitalize on the high overpotential on the carbon surface to kinetically slow down hydrogen generation. Nevertheless, hydrogen generation is a thermodynamic reality in VFBs. Even more of a concern for long-term cycling is the potential of the V^{2+}/V^{3+} redox reaction to become more negative as the state of charge (SoC) increases, thereby elevating the driving force for the HER.[18] The generated hydrogen not only blocks electrolyte access to the surface of the carbon electrode but also introduces mass and valence imbalances at the two electrodes, resulting in capacity decay and low energy efficiency.[23, 24] Accumulation of hydrogen gas generated in the negative half-cell reservoir could become a potential safety hazard. Very little research has been done to investigate HER behaviors during real battery operations, with most of the research focusing on mitigating hydrogen generation and accumulation.[15, 16, 25, 26] A study documenting quantitative ex situ measurement to determine the HER rate occurring at two different negative carbon paper electrodes was published,[16] and the results demonstrated that the surface chemistry (e.g., functional groups), porosity, and surface area of the carbon electrode were the main factors that determines the hydrogen formation rate. An *in-situ* investigation also reported observations of HER behaviors.[18] A transparent battery was designed to visualize and record hydrogen gas bubbles during battery operation. While the results of that research provide an

understanding of the hydrogen generation rate and effects of electrode materials on the HER, there has been no report on the prediction and detection of hydrogen generation as well as SoC of negative electrolyte during flow battery operations. Considering the SoC swing during the operation of a VFB, a low-cost portable hydrogen detection device will be important to provide real-time SoC and hydrogen generation information to the battery management system for operation control. A hydrogen gas detector in the electrolyte reservoir can warn when the hydrogen gas level in the headspace has reached a certain level. Yet, a non-invasive technology that can provide predictions and warnings of the in situ/operando hydrogen generation is still lacking.

In this work, we developed an ultrasonic probing approach for monitoring the SoC of VFBs and the hydrogen bubbles as well as predicting the hydrogen evolution in a negative half-cell of a VFB, thus providing an indicator of hydrogen generation during battery operation to mitigate the risk of hydrogen accumulation. In a previous study, we developed a similar ultrasonic probing approach for monitoring the SoC of VFBs in a positive half-cell.[27] In this paper, we demonstrated that our ultrasound diagnostic approach has a great potential for obtaining real-time SoC measurements in the negative electrolyte of a VFB. At the same time, due to the competitive reaction between vanadium redox reaction and hydrogen evolution, we may provide a possible method to predict the hydrogen evolution by the trend of SoC change during battery operation. Furthermore, in an online experiment, we successfully detected gas bubbles via acoustic measurements when the flow battery was in operando.

2. Method

2.1. Device

An acoustic probing system was designed to detect hydrogen bubbles in the anolyte solution of VFBs. It consists of a custom designed ultrasonic probing cell made of borosilicate glass that can

be integrated into the flow system on the anolyte side (Figure 1). An ultrasonic transducer controlled by an ultrasonic pulser receiver is attached to the probing cell, and the pulser receiver is connected to a computer. Control commands are sent from the computer to the pulser receiver while data are transmitted from the pulser receiver back to the computer for analysis. During the charging-discharging cycling, the anolyte solution flows through the negative electrode, where the redox reaction occurs. Under extreme conditions, hydrogen bubbles are generated at the negative electrode. The electrolyte solution consisting of hydrogen gas bubbles then flows into the ultrasonic probing cell. The ultrasonic transducer, which is attached to the sidewall of the glass cell, generates signals that can propagate into the probing cell and receives echoes. Since the echoes have propagated through the electrolyte solution in the probing cell, they can provide information about the acoustic properties of the solution. Details about how the signals are transmitted and how the pulser receiver is configured were described in a previous publication.[27] Echoes are received by the ultrasonic receiver and processed on the computer using signal processing methods. The sound speed and acoustic attenuation coefficient are calculated from the echoes (detailed methods for these calculations are described in a previously published paper).[27] Bubbles formed in the electrolyte solution flow through the acoustic path and are reflected as abnormal values in measurements of the sound speed and attenuation coefficient. The ultrasonic system can monitor bubbles continuously in negative electrolytes without interrupting battery operation, thus providing real-time noninvasive surveillance of the health of flow battery systems.

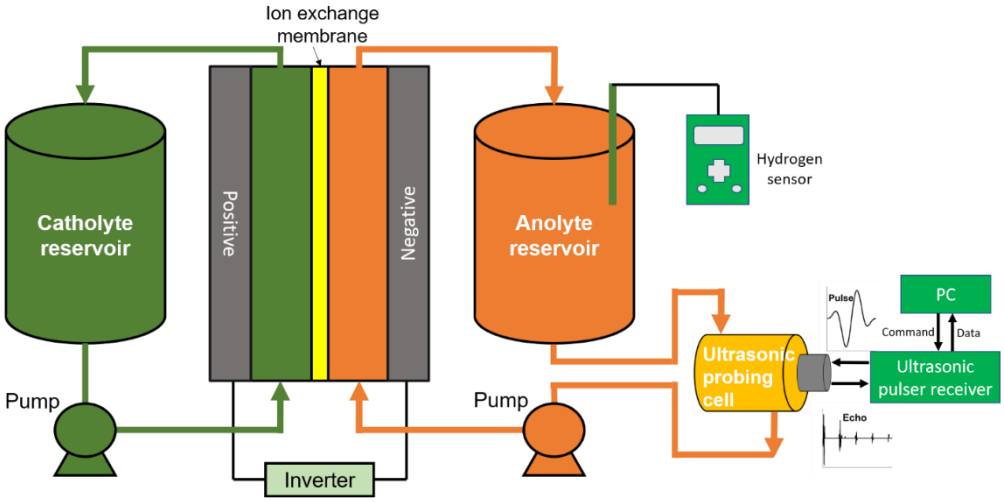

Figure 1. Schematic of the in-situ battery health monitoring system for hydrogen detection in an all-vanadium redox flow battery.

2.2 Hydrogen bubble detection

2.2.1 Experiment setup

Static offline experiment

Typical vanadium flow battery electrolytes (1.5M $VOSO_4$ + 3.5M H_2SO_4 aqueous solutions) used in static and operando tests were prepared using specific amounts of highly concentrated sulfuric acid (Sigma, ~98%), $VOSO_4$ xH_2O compound (NOVA), and deionized water. The mass of elemental vanadium in the $VOSO_4$ xH_2O was analyzed using inductively coupled mass spectroscopy (Perkin Elmer Optima 7300 DV). The flow cell with an active electrode area of 10 cm^2 (2 cm × 5 cm) consists of a Solvay (thickness ~93 um) cation exchange membrane and porous carbon as the cation exchange membrane and electrodes for positive and negative sides, respectively. The V^{3+} electrolyte solution was prepared at the negative side by charging 1.5M $VOSO_4$ + 3.5M H_2SO_4 aqueous solutions.

To examine the validity of the designed acoustic probing techniques for detection of bubbles in a liquid, two offline static experiments were performed with deionized water and a negative electrolyte solution. The static experiments were performed by injecting hydrogen gas into the ultrasonic probing cell at varying gas flow rate (2, 4, 6, 8, and 10 cc/min). In each experiment, the deionized water and the electrolyte solution were pumped into the acoustic measurement cell. Water circulation was stopped after the acoustic measurement cell was fully filled with either the deionized water or the electrolyte, and then hydrogen gas was injected into the cell through a thin plastic tube (0.5 mm diameter) inserted into the inlet. The inlet then was sealed to prevent leakage of any liquid. At each gas flow rate, acoustic measurements were repeated 500 times at 10-second intervals.

In-situ online experiment with validation

The *in-situ* test setup of a flow cell for hydrogen gas bubble monitoring with a cylindrical measurement cell in the flow path on the anolyte side is similar to the setup we used in a previously reported study.[27] The cycling test at a cut-off potential window between (0.8 V and 1.6 V) was performed prior to the hydrogen bubble test to guarantee the normal operation of the cell. For the charging process at the 21st cycle, the voltage applied on the cell was increased to 1.8 V, 1.9 V, and 2.0 V. The cell voltages were held at each of those voltages for around 15 minutes. As the applied voltage increases on the flow cell, the current density will increase, and the potential at the negative electrode will become more negative, which will lead to the generation of more hydrogen gas bubbles. We used a hydrogen detector (HY-ALERTA™ 500, H2scan, California, USA) to validate the generation of hydrogen gas in the negative electrolyte solution. The headspace of the

V^{2+}/V^{3+} electrolyte reservoir was connected to the hydrogen sensor with stainless tubing (Figure S1 in the Supplemental Information [SI]).

2.2.2 Data processing

The sound speed and acoustic attenuation coefficient of each liquid tested was calculated from received waveforms.[27] Bubbles were denoted by abnormal values and large variabilities in the sound speed and the acoustic attenuation coefficient of the negative electrolyte. When a bubble passes through the propagation path of sound waves, it creates a discontinuity in the sound propagation medium. The sound speed in a gas is slower than in a liquid, thus leading to a difference in the travel time of the sound waves. Meanwhile, sound waves are scattered by bubbles, causing energy loss in the original propagation direction. Thus, in the presence of bubbles, measurements of both the sound speed and the acoustic attenuation coefficient will have different values than would be detected when no bubbles were present in the electrolyte. The frequency of abnormal values depends on the generation speed of bubbles; that is, the number of bubbles generated at the negative electrodes. The variability of both sound speed and attenuation coefficient, such as standard deviation (std) and interquartile range (IQR), were calculated, and their correlations with gas flow rate were explored to understand the quantitative relationships between gas flow rate and variability of acoustic measurements. These quantitative relationships serve as an indicator of the amount of gas bubbles generated in the VFB negative electrolyte.

3. Results and discussion

3.1 Offline experiments

Sound speeds and attenuation coefficients were presented in boxplots for deionized water (Figure 2) and anolyte solutions (Figure 3). In each box, the central mark indicates the median, and the

bottom and top edges of the box indicate the 25th percentile (Q1) and 75th percentile (Q3), respectively. The difference between Q3 and Q1 are the interquartile ranges. Whiskers that extend to the most extreme data points (maximum: Q3 + 1.5*IQR, minimum: Q1 -1.5*IQR) are not considered outliers. Outliers that were observed are plotted using '+' symbols.

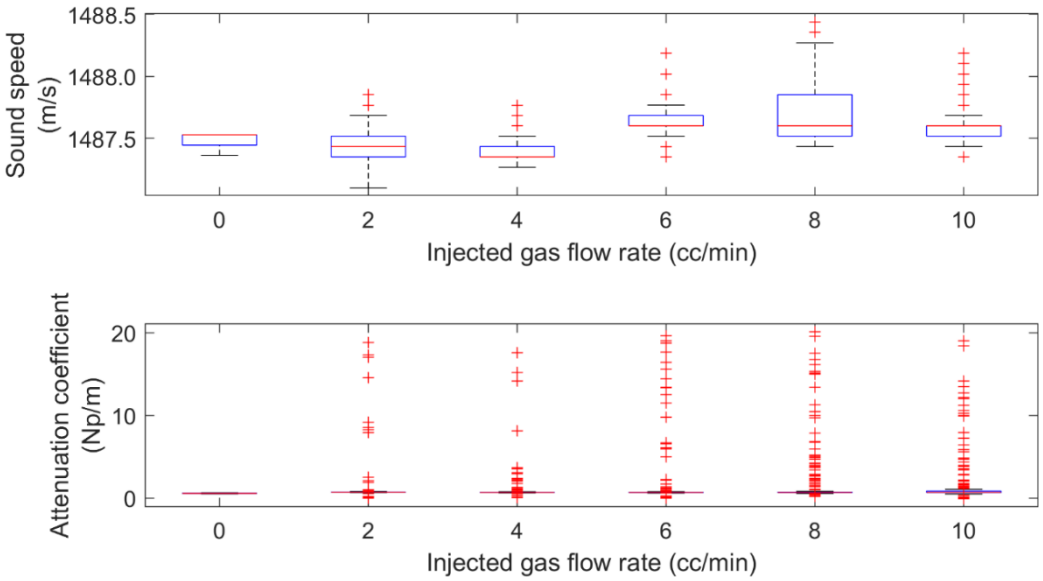

Figure 2. Boxplots of the sound speed and acoustic attenuation coefficient at different gas flow rate in deionized water.

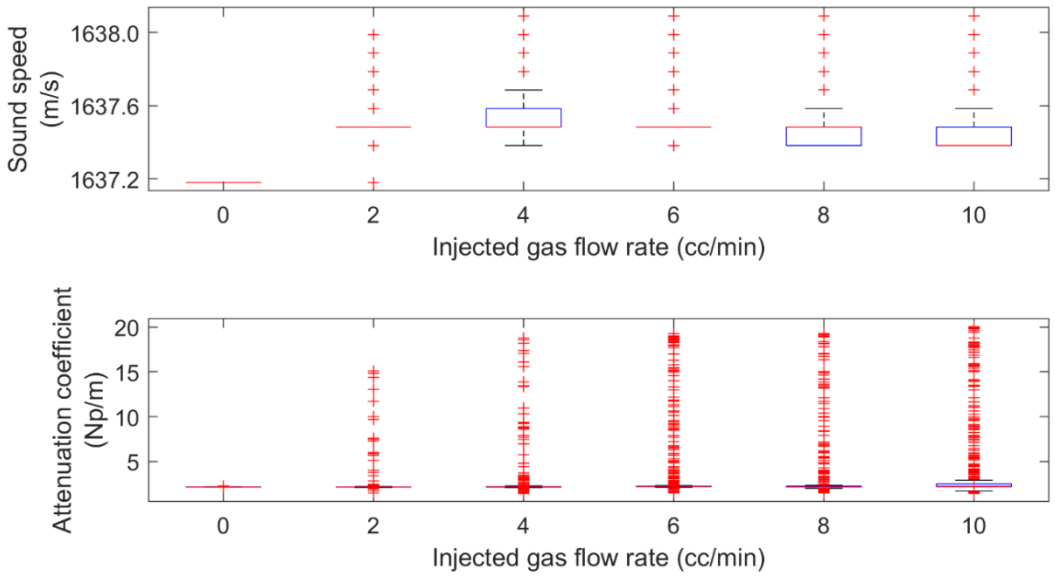

Figure 3. Sound speed and acoustic attenuation coefficient at different gas flow rate in anolyte solution.

In the boxplots in Figure 2 and 3, bubbles can be represented as outliers (denoted by red '+' symbols) and/or increased interquartile ranges (the difference between two whiskers denoted by black bars), both of which demonstrate increased variability in acoustic measurements of the anolyte solution. When no bubbles exist in the fluid, there are no outliers in both sound speed and attenuation coefficient, and the interquartile range is very small. Depending on how sound speed measurements are distributed, cases where median values overlap with the box edge occur when the median value is equal to the first/third quartile values.

Figures of all sound speed and acoustic attenuation coefficient samples in both water and electrolyte solution tests are included in the SI (Figures S2–S5). When hydrogen gas was injected into the test fluid, we observed many outliers in both sound speed and attenuation coefficient measurements, and the IQR is larger than that observed for no gas cases. Moreover, the IQR and number of outliers generally increase as the gas flow rate increases, indicating that more bubbles

are detected by acoustic measurements at higher gas flow rates. We also found that the attenuation coefficient measurement seems more sensitive to gas bubbles, as indicated by the presence of many more outliers than found in sound speed measurements at the same gas flow rate. Overall, when hydrogen gas was injected into the electrolyte solutions, the variabilities of both sound speed and attenuation coefficient were much higher than when no gas was injected.

To quantify the relationship between variations of electrolyte acoustic properties and injected gas flow rates, the std and IQR were correlated with the gas flow rates. The correlation coefficients with corresponding p-values are listed in Table 1.

Table 1. Correlation coefficients between two statistic metrics (std: standard deviation; IQR: interquartile range) of acoustic properties and the injecting gas flow rates in deionized water and the vanadium negative electrolyte solution.

Testing Liquid	Acoustic Properties	Correlation Coefficient between std and Gas Flow Rate	Correlation Coefficient between IQR and Gas Flow Rate
Deionized water	Sound speed	0.67 (p = 0.15)	0.77 (p = 0.08)
	Attenuation coefficient	0.92 (p = 0.01)	0.79 (p = 0.06)
Vanadium negative electrolyte solution	Sound speed	0.89 (p = 0.02)	0.68 (p = 0.13)
	Attenuation coefficient	0.95 (p = 0.00)	0.80 (p =0.06)

For the test in deionized water, the linear correlation is statistically significant ($p<0.05$) for attenuation coefficient, with 0.92 correlation coefficient between the std and gas flow rate. For the test in the anolyte solution, the linear correlation is statistically significant ($p<0.05$) both the std of the sound speed and the std of the attenuation coefficient. In summary, for both deionized water and vanadium electrolyte solutions, the standard deviation of the attenuation coefficient are linearly correlated with the flow rate of injected gas. Linear correlations between variability (both std and IQR) of acoustic measurements and the gas flow rate provide strong indicators of the

amount of gas bubbles in the anolyte solution. This relationship would be very helpful for detecting the amount of hydrogen gas generation and managing operational battery health.

3.2 Online experiment

Before hydrogen bubble testing, cycling tests was performed for the cell in a 0.8 V–1.6 V potential window. Almost no charge/discharge capacity loss was observed, and the ~1.45 Ah capacity could be maintained over the first 20 cycles (Figure 4.a and 4.b). Figure 4.c shows the columbic efficiency (CE) and energy efficiency (EE) results obtained during cycling tests for the investigated battery. The CE and EE were maintained at ~99% and ~87% for the first 20 cycles, respectively. The stable battery performance during cycling indicates that the investigated battery operated normally. In addition, the sound speed (Figure 5.a) and attenuation coefficient (Figure 5.b) periodically varied during the first 20 charge/discharge cycles. Figure 5.a and Figure 5.b also show that sound speed and attenuation coefficient linearly decrease with the SoC, which linearly increases with increasing charge time at each cycle. Considering that there is no side reaction such as hydrogen evolution below the cut-off potential of 1.6 V, it is noted here that the capacity utilization of 75% (calculated by charge time multiplied by charge current) in this flow battery test is the maximum SoC we can achieve. Since sound speed is more sensitive to temperature and other uncontrollable factors such as crossover between positive and negative electrolytes, fluctuations of sound speed between different cycles could be observed as cycling. In contrast, the attenuation coefficient is very stable with cycling, which linearly decreases from 2.145 Np/m to 1.691 Np/m as the SoC increases from 0 to 75%. With the two SoC data points and corresponding attenuation coefficients, we can establish the linear relationship between the SoC and the attenuation coefficient as $SOC = -1.652\alpha + 3.542$, where α represents the attenuation coefficient. Using this relationship, we can estimate the SoC given any observed attenuation

coefficient α. For example, the estimated SoC is 50% when the measured attenuation coefficient is1.842 Np/m. The stable cycling curves shown in Figures 5.b clearly show that our ultrasonic probing system can monitor the SoC of the negative electrolyte.

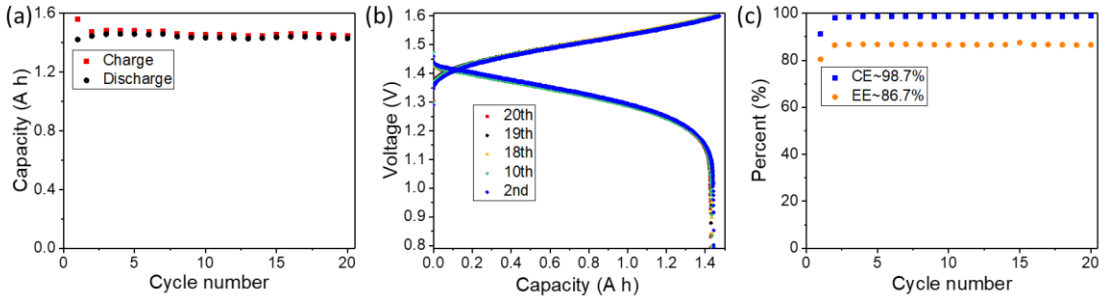

Figure 4. Cycling testing of the investigated battery. (a) Charge/discharge capacity as cycling progresses. (b) Charge/discharge voltage profiles at different cycles. (c) CE and EE.

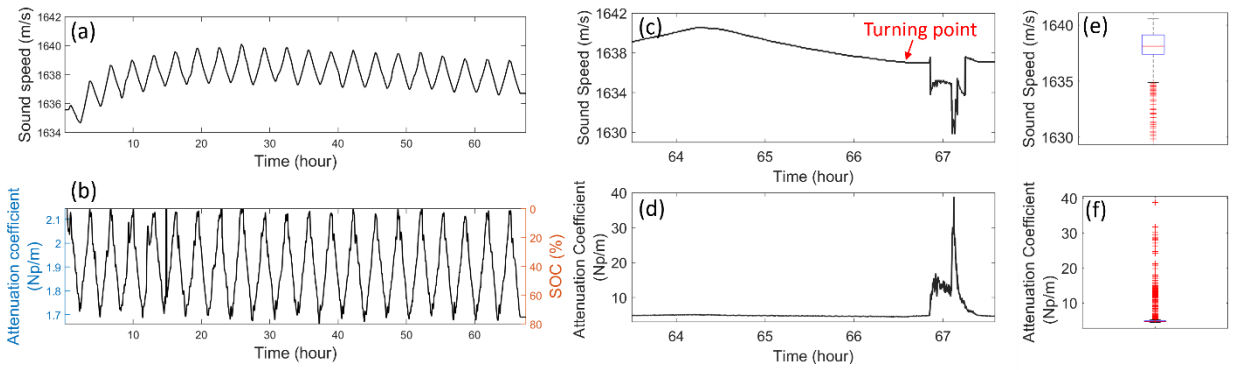

Figure 5. In situ bubble detection experiment results when hydrogen bubbles were generated by extreme voltage levels. a) Sound speed during the first 20 cycles under normal condition. b) Acoustic attenuation coefficient and corresponding state of charge (SoC) of the first 20 cycles under normal conditions. c) Abrupt decrease in sound speed observed after the extreme voltage was enforced. Note that c) and a) are the same test at different voltage conditions, but the two plots are displayed in different scales to show the clear cycling pattern under normal operation and the large variability under extreme condition, respectively. d) Abrupt increase in attenuation coefficient after the extreme voltage was enforced. Note that d) and b) are the same test at different voltage conditions, and the two plots are displayed in different scales to show the clear cycling pattern under normal operation and the large variability under extreme conditions, respectively. e) Boxplot of sound speed shows outliers that are smaller than the minimum sound speed under normal operation conditions. f) Boxplot of attenuation coefficient shows outliers that are larger than the maximum attenuation coefficient under normal operation conditions.

In the 21st cycle of the charging process at a constant current density of 75 mA/cm^2, we found the change in the sound speed (Figure 5.c) and attenuation coefficient (Figure 5.d) to be linear over the first two hours (from hour 64.25 to hour 66.25), which indicates that the main contribution of the V^{2+}/V^{3+} redox reaction is at negative side. Note that results shown in Figure 5.a and Figure 5.c are for the same test but at different voltage conditions. The two plots are displayed in different scales to show the difference between the clear cycling pattern under normal operations (Figure 5.a) and when large variability occurs under extreme conditions (Figure 5.c). The same thing is true for the attenuation coefficient results shown in Figure 5.b and Figure 5.d. After 2 hours charging, the charge capacity reached 1.5 Ah, and the capacity utilization was almost 90%. At hour 66.58, the sound speed curve reaches a turning point where the slope changes abruptly from -0.3 to 0 because the variation of sound speed plateaued for 15 minutes (i.e., the slope of sound speed curve was unchanged) (Figure S6 in SI). Theoretically, only two reactions can occur at the negative side during the charge process—the V^{2+}/V^{3+} redox reaction and hydrogen evolution. The 15-minute plateau is an indication that hydrogen generation had started, although the acoustic measurement was not able to detect the gas bubbles during that period. It is noted that the charge voltage was nearly 1.7 V after charging for 2 hours.

After the flow cell was charged to 1.8 V, the applied voltage of 1.8 V was retained for about 15 minutes (from hour 66.58 to hour 66.85). The sound speed and attenuation coefficient were maintained at constant levels, and no abrupt decreases/increases were observed (Figure 5.c and Figure 5.d). Therefore, during the time period when the cell was maintained at 1.8 V, V^{2+}/V^{3+} redox reaction happened at negative side was limited because no changes in sound speed and attenuation coefficient were observed, which indicates that hydrogen evolution is the main reaction

that occurs at the negative electrode at this voltage, although again, no hydrogen gas bubbles could be detected by our acoustic detector. Generally, the small amount of hydrogen bubbles initially adsorbed on the electrode then coalesced to form a bubble that was large enough to be released into the flowing electrolyte and detected by our acoustic detector. The absence of a large bubble flowing through the glass cylinder during the time when the cell was maintained at 1.8 V is possibly the reason no hydrogen was detected. Another possible reason is that a small amount of hydrogen in small bubbles could not be detected by our acoustic detector. We expect that in commercial flow battery systems, where the electrode size would be much larger than those at laboratory scale, hydrogen bubbles can aggregate more rapidly and can be detected earlier than in the laboratory experiments.

When we increased the charge cutoff voltage from 1.8V to 1.9 V at hour 66.85, large gas bubbles were observed visually and were detected by acoustic measurements (Figure 5.c and Figure 5.d). For sound speed, when higher voltage was enforced, sound speeds abruptly decreased for about 25 minutes. Simultaneously, the attenuation coefficient abruptly increased. The boxplot of sound speeds (Figure 5.e) shows many outliers with speeds that are lower than the minimum sound speed observed under normal conditions, while the boxplot of attenuation coefficients (Figure 5.f) shows many outliers that are larger than the maximums observed under normal conditions. The appearance of hydrogen gas bubbles was validated by the HY-ALERTA™ 500 hydrogen detector (Figure S1 in the SI) that was installed in a flow battery system. A valve was installed in electrolyte flow path and flashing red rights on the sensor observed just after the valve was opened indicated the presence of hydrogen in the flowing electrolyte.

Based on the results of the offline static experiments (denoted by blue stars in Figure 6), a linear relationship (the black dashed line in Figure 6) between the flow rate and the std of the attenuation

coefficient was established. Since the std is a statistical metric that can measure the amount of variation of the whole dataset, it is more appropriate to be used to estimate the flow rate than the IQR, which only denotes the range of the middle 50% of the dataset. The linear relationship was then used to estimate the hydrogen flow rate of the in-situ experiment. The attenuation coefficient measurements between hours 66.85 to 67.27, during which time bubbles were visually observed in the glass measurement cell, were extracted and their std value was calculated as 5.99 Np/m. Inserting the std value to the linear relationship yielded a flow rate of 13.50 cc/min, i.e., the estimated average hydrogen gas flow rate during the *in-situ* experiment is 13.50 cc/min. The primary factor influencing the rate of hydrogen production is the buildup of gas bubbles on the graphite electrode. This accumulation creates significant pressure, leading to a high flow rate of gas bubbles upon release. However, these bubbles are non-continuous, resulting in intermittent release. During our in-situ experiments, we observed the formation of a sizable bubble cloud approximately every 40 seconds. In contrast, in static experiments, the gas bubbles consistently flowed through our transducer at a constant speed. It should be noted that the linear relationship only crudely estimated the hydrogen gas flow rate since the bubbles generated in the *in-situ* experiments were in different sizes from the static offline experiments. During the offline experiments, gases were injected into the solution through a tube, and the gas bubbles have larger diameters (approximately 3 mm by visual estimation). While in the in-situ experiments, the bubbles were of a smaller size (approximately 1 mm by visual estimation). Bubbles in offline experiments aligned like a bead chain-while in the *in-situ* experiments small bubbles aggregated in the form of clouds. Despite of the difference in bubble size and forms, the std of attenuation coefficient is still a good quantitative metric to estimate the flow rate of hydrogen gas generated

in the negative electrolyte, and the acoustic detection approach is a robust noninvasive method that can monitor the hydrogen generation levels quantitatively.

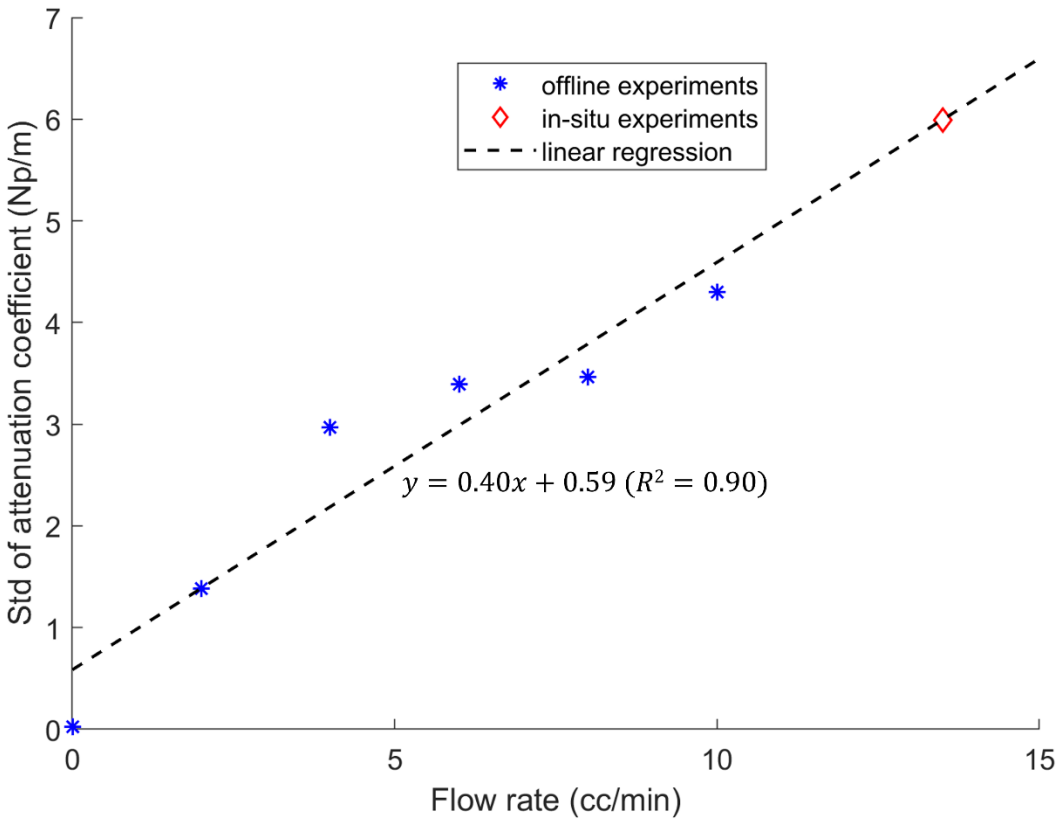

Figure 6. Linear regression between the hydrogen gas flow rate and the standard deviation (std) of the attenuation coefficient of the negative electrolyte measured in the offline experiments. The linear relationship was then used to estimate the hydrogen gas flow rate from the std of attenuation coefficient of the in-situ experiments (red diamond).

In summary, we have developed a method for predicting and monitoring hydrogen generation in VRBs during the charging process. Although the acoustic measurement cannot detect the hydrogen bubbles during the very early stage of hydrogen generation (i.e., when the applied voltage was <1.8 V), our acoustic measurement approach can provide early indications/predictions of hydrogen

generation by identifying changes in the sound speed slope at the onset of the hydrogen generation. Moreover, when a higher voltage was applied, an abrupt decrease in sound speed and an abrupt increase in attenuation clearly indicate hydrogen gas bubbles generation. We found that the standard deviation of the attenuation coefficient has a linear relationship with hydrogen bubble amounts and flow rates. With more ultrasonic measurements of charge-discharge cycling at the negative half-cell, we will develop machine learning models to build a robust and comprehensive tool to predict and monitor the state of charge and state of health monitoring of VRBs.

4. Conclusion

We have designed a noninvasive technology that uses an ultrasonic pulse-echo method to monitor SoC of anolyte, predict the hydrogen generation and detect hydrogen gas bubbles in VFB anolyte solutions. The technology has the advantages of being fast and reliable, and it does not interfere with operation of flow batteries. There currently is a resurgence of interest in the use of redox flow batteries for large-scale energy storage because they can provide some critical services in many grid energy applications; for example, providing premium back-up power, balancing daily energy time shifts, and improving grid reliability. However, hydrogen generation is a common concern for various redox flow chemistries, such as VFBs and iron-chromine flow batteries. This hydrogen generation, which occurs during the charging process, presents a potential safety hazard challenge during operations.

Our in-situ health monitoring technology is a low-cost system that can provide early prediction and real-time detection of hydrogen bubbles and SoC, which can aid flow battery safety management and ultimately increase flow battery reliability. Through measurements of sound speed and acoustic attenuation coefficient of the negative electrolyte solution, we found that the point at which the change in attenuation and sound speed becomes nonlinear with SoC is a strong

indicator of hydrogen generation. The appearance of hydrogen gas bubbles can be detected immediately, and the amount of gas bubbles is highly correlated with variabilities of the measured acoustic properties.

Acknowledgement

X.Z. and L.Y. contributed equally to this work. The authors would like to acknowledge financial support from the U.S. Department of Energy (DOE) Office of Electricity Energy Storage Program (under Contract No. 70247). The idea originated from another project funded by DOE's Water Power Technologies Office. Pacific Northwest National Laboratory is operated by Battelle for DOE under Contract DE-AC05-76RL01830.

References

1. M. Schreiber, M. Harrer, A. Whitehead, H. Bucsich, M. Dragschitz, E. Seifert and P. Tymciw, *Journal of Power Sources*, 2012, **206**, 483-489.
2. Z. Yang, J. Zhang, M. C. W. Kintner-Meyer, X. Lu, D. Choi, J. P. Lemmon and J. Liu, *Chemical Reviews*, 2011, **111**, 3577-3613.
3. M. Park, J. Ryu, W. Wang and J. Cho, *Nat. Rev. Mater.*, 2016, **2**, 16080.
4. B. Dunn, H. Kamath and J.-M. Tarascon, *Science*, 2011, **334**, 928-935.
5. W. Wei, L. Qingtao, L. Bin, W. Xiaoliang, L. Liyu and Y. Zhenguo, *Adv. Funct. Mater.*, 2013, **23**, 970-986.
6. M. Pugach, M. Kondratenko, S. Briola and A. Bischi, *Applied Energy*, 2018, **226**, 560-569.
7. Y. Shi, C. Eze, B. Xiong, W. He, H. Zhang, T. M. Lim, A. Ukil and J. Zhao, *Applied Energy*, 2019, **238**, 202-224.
8. M. Skyllas-Kazacos, L. Cao, M. Kazacos, N. Kausar and A. Mousa, *ChemSusChem*, 2016, **9**, 1521-1543.
9. M. Skyllas-Kazacos, M. H. Chakrabarti, S. A. Hajimolana, F. S. Mjalli and M. Saleem, *Journal of The Electrochemical Society*, 2011, **158**, R55.
10. L. Estevez, D. Reed, Z. Nie, A. M. Schwarz, M. I. Nandasiri, J. P. Kizewski, W. Wang, E. Thomsen, J. Liu, J.-G. Zhang, V. Sprenkle and B. Li, *ChemSusChem*, 2016, **9**, 1455-1461.
11. B. Li, M. Gu, Z. Nie, Y. Shao, Q. Luo, X. Wei, X. Li, J. Xiao, C. Wang, V. Sprenkle and W. Wang, *Nano Lett.*, 2013, **13**, 1330-1335.
12. L. Li, S. Kim, W. Wang, M. Vijayakumar, Z. Nie, B. Chen, J. Zhang, G. Xia, J. Hu, G. Graff, J. Liu and Z. Yang, *Advanced Energy Materials*, 2011, **1**, 394-400.
13. D. Reed, E. Thomsen, W. Wang, Z. Nie, B. Li, X. Wei, B. Koeppel and V. Sprenkle, *Journal of Power Sources*, 2015, **285**, 425-430.
14. W. Wang, Z. M. Nie, B. W. Chen, F. Chen, Q. T. Luo, X. L. Wei, G. G. Xia, M. Skyllas-Kazacos, L. Y. Li and Z. G. Yang, *Adv. Energy Mater.*, 2012, **2**, 487-493.
15. C.-N. Sun, F. M. Delnick, L. Baggetto, G. M. Veith and T. A. Zawodzinski, *Journal of Power Sources*, 2014, **248**, 560-564.
16. R. Schweiss, A. Pritzl and C. Meiser, *Journal of The Electrochemical Society*, 2016, **163**, A2089-A2094.
17. F. Chen, S. Gu, Q. Ma, Q. Liu and M. Zhang, *Journal of The Electrochemical Society*, 2017, **164**, A2403-A2406.
18. L. Wei, T. S. Zhao, Q. Xu, X. L. Zhou and Z. H. Zhang, *Applied Energy*, 2017, **190**, 1112-1118.
19. L. Eifert, Z. Jusys, R. J. Behm and R. Zeis, *Carbon*, 2020, **158**, 580-587.

20. D. Aaron, C. N. Sun, M. Bright, A. B. Papandrew, M. M. Mench and T. A. Zawodzinski, *ECS Electrochemistry Letters*, 2013, **2**, A29-A31.
21. C. N. Sun, F. M. Delnick, D. S. Aaron, A. B. Papandrew, M. M. Mench and T. A. Zawodzinski, *ECS Electrochemistry Letters*, 2013, **2**, A43-A45.
22. S. Kim, E. Thomsen, G. Xia, Z. Nie, J. Bao, K. Recknagle, W. Wang, V. Viswanathan, Q. Luo, X. Wei, A. Crawford, G. Coffey, G. Maupin and V. Sprenkle, *Journal of Power Sources*, 2013, **237**, 300-309.
23. E. Agar, C. R. Dennison, K. W. Knehr and E. C. Kumbur, *Journal of Power Sources*, 2013, **225**, 89-94.
24. A. A. Shah, H. Al-Fetlawi and F. C. Walsh, *Electrochimica Acta*, 2010, **55**, 1125-1139.
25. D. J. Suárez, Z. González, C. Blanco, M. Granda, R. Menéndez and R. Santamaría, *ChemSusChem*, 2014, **7**, 914-918.
26. X.-Z. Yuan, C. Song, A. Platt, N. Zhao, H. Wang, H. Li, K. Fatih and D. Jang, *International Journal of Energy Research*, 2019, **43**, 6599-6638.
27. X. Zang, L. Yan, Y. Yang, H. Pan, Z. Nie, K. W. Jung, Z. D. Deng and W. Wang, *Small Methods*, 2019, **3**, 1900494.